Article

Evidence of Excited-State Vibrational Mode Governing the Photorelaxation of a Charge-Transfer Complex

Published as part of The Journal of Physical Chemistry A virtual special issue "Gregory A. Voth Festschrift".

Federico Coppola, Paola Cimino, Alessio Petrone, and Nadia Rega*

ACCESS | Metrics & More | Article Recommendations | SI Supporting Information

ABSTRACT: Modern, nonlinear, time-resolved spectroscopic techniques have opened new doors for investigating the intriguing but complex world of photoinduced ultrafast out-of-equilibrium phenomena and charge dynamics. The interaction between light and matter introduces an additional dimension, where the complex interplay between electronic and vibrational dynamics needs the most advanced theoretical−computational protocols to be fully understood on the molecular scale. In this study, we showcase the capabilities of ab initio molecular dynamics simulation integrated with a multiresolution wavelet protocol to carefully investigate the excited-state relaxation dynamics in a noncovalent complex involving tetramethylbenzene (TMB) and tetracyanoquinodimethane (TCNQ) undergoing charge transfer (CT) upon photoexcitation. Our protocol provides an accurate description that facilitates a direct comparison between transient vibrational analysis and time-resolved spectroscopic signals. This molecular level perspective enhances our understanding of photorelaxation processes confined in the adiabatic regime and offers an improved interpretation of vibrational spectra. Furthermore, it enables the quantification of anharmonic vibrational couplings between high- and low-frequency modes, specifically the TCNQ "rocking" and "bending" modes. Additionally, it identifies the primary vibrational mode that governs the adiabaticity between the ground state and the CT state. This comprehensive understanding of photorelaxation processes holds significant importance in the rational design and precise control of more efficient photovoltaic and sensor devices.
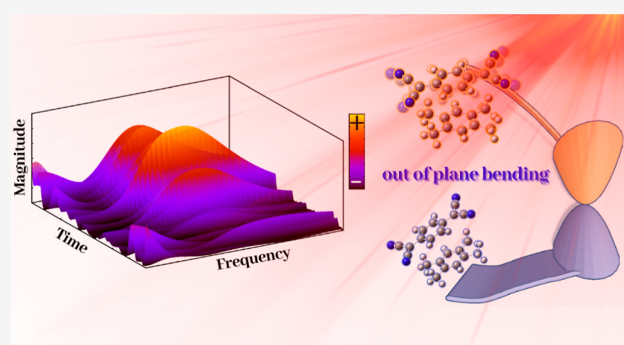
INTRODUCTION

Photoinduced charge-transfer (CT) reactions are of paramount importance across a spectrum of scientific domains, notably encompassing chemistry, biology, and materials science.[1−7] The complex interplay between nuclear motions and electronic rearrangement upon excitation requires the most advanced spectroscopic and computational techniques to be fully understood. The Born−Oppenheimer approximation, which conveniently separates electronic and nuclear motions and the subsequent potential energy surface (PES) definition and exploration by theoretical methods (i.e., geometry optimizations and molecular dynamics), becomes often a starting point for more advanced techniques required to better understand photoinduced CT and nonequilibrium phenomena. These are crucial to be studied in the more critical PES regions where nonadiabatic effects are prominent, such as avoided crossings (ACs) and conical intersections (CIs).[8−11] At such pivotal geometrical locations, the nonadiabatic couplings between involved electronic states are key factors to guide the investigations. In these regions, where the nuclear and electronic motions are strongly entangled, it is possible to enable efficient nonradiative relaxation channels, contributing to ultrafast electronic and vibrational relaxations, population exchanges, and radiationless transitions between electronic states.[12−15] These processes are usually ultrafast (typically last less than 100 fs) and critically influence the rates and ultimate products of numerous photochemical molecular events.[16−21]

A deep knowledge of the PES regions around CIs (since CIs themselves are rare to be encountered directly) is critical since nonadiabatic phenomena are ubiquitous in the photophysics and photochemistry of a broad set of photoactive molecules, encompassing biopolymer components[22−27] and novel photovoltaic materials.[28−34] Various spectroscopic techniques have emerged as powerful tools for monitoring electronic wave packet dynamics in proximity to nonadiabatic CI regions, including two-dimensional electronic−vibrational spectroscopy
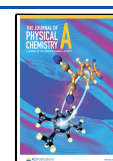
and femtosecond stimulated Raman spectroscopy.[12,35−41] These methods facilitate the correlation of electronic and nuclear degrees of freedom, especially during the initial stages of the photon absorption and subsequent nuclear rearrangement.[35−38] Femtosecond stimulated Raman spectroscopy is a particularly favored method for studying vibrational coherence in molecular systems within nonadiabatic regions.[39−41] Transient absorption spectroscopy represents another crucial tool for monitoring the vibrational wave packet dynamics in proximity to points or seams of PES degeneracy, as observed during singlet exciton fission and excited-state (ES) isomerization events.[29,42,43] In addition, the advent of attosecond spectroscopic techniques has paved the way for the mapping of wave packet bifurcation and the discernment of curve crossings.[44−49] These advances have significantly expanded the exploration of a wide array of physical phenomena, spanning from the dynamics of large protein assemblies tumbling in the nanosecond domain to the ultrafast electron dynamics occurring on attosecond time scales.

However, bridging the gap between time-resolved experiments and their molecular interpretations via theory and computation is still a challenge. While the rigorous depiction of femtochemistry in photoexcited systems on a molecular scale is rendered feasible through quantum dynamics simulations[50−52] or quantum classical techniques,[53−58] their limitations are primarily linked to hardware capabilities and the substantial memory requirements, which impact the duration of simulations and the size of systems that can be effectively studied. These limitations are particularly noticeable when large biologically or technologically relevant systems are investigated within realistic environments. Nevertheless, it is worth noting that these methods remain valuable for providing a precise understanding of the fundamental physics underlying the studied phenomena.[59−64] It is also worth noting that these methods dealing with statistical averages or mean field potentials require still theoretical developments for providing a direct connection with time-resolved spectroscopic data.

On the other hand, plenty of information can be indeed inferred by out-of-equilibrium vibrational relaxation on highly accurate ab initio defined single PESs, enabling the modeling of light−matter interactions and subsequent relaxation dynamics for interpretative purposes and the acquisition of useful insights that may be experimentally elusive. Thus, in this work, we propose an extensive theoretical characterization of a model system for photoinduced CT and its nonequilibrium dynamics, both in the ground state (GS) and first singlet ES. We propose to employ density functional theory (DFT) and its time-dependent version (TD-DFT) to focus on photophysical and photoreactive events using a theoretical−computational protocol developed by us for transient vibrational analysis to provide a molecular interpretation for time-resolved experiments.[61,65−71] The protocol combines ab initio molecular dynamics simulations[72−78] and wavelet transform[69,71,79−81] to examine the time evolution of structural changes in both electronic states, particularly the rearrangement of nuclei to the new electronic density of the CT state and their ultrafast relaxation from the Franck−Condon region. In particular, we focus on the time-resolved vibrational characterization of a noncovalent CT dimer: a donor molecule, 1,2,4,5-tetramethylbenzene (TMB), and an acceptor molecule, 7,7,8,8-tetracyanoquinodimethane (TCNQ, see Figure 1).

TCNQ is a versatile electron acceptor due to its high electron affinity and its ability to form CT complexes with
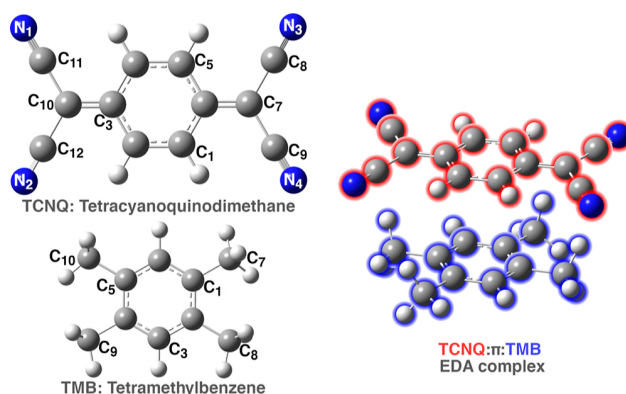

Figure 1. Subunits forming the CT complex (TMB, bottom left, and TCNQ, top left) with labeling scheme and side view of the TMB:π:TCNQ electron-donor/acceptor (EDA) complex. Carbons are reported in gray, hydrogens in white, and blue is for nitrogens.

various electron donors, making it relevant in solid-state chemistry research.[82−90] Time-resolved experimental data[91] suggests the presence of a tuning mode and a coupling mode to form the CI and describes the branching space of the nonadiabatic transition, and the vibrational coupling plays a critical role in modulating charge recombination even in the GS, although a full comprehension is still far to be achieved. In detail, femtosecond stimulated Raman spectroscopy has been employed by Mathies and co-workers to explore the vibrational dynamics of the photoinduced CT within this noncovalent electron-donor/acceptor complex.[41,91] In solution, the TMB-π-TCNQ complex exhibits a broad, featureless CT absorption band in the range of 600−450 nm, primarily characterized by an intermolecular excitation from the highest occupied molecular orbital (HOMO) of TMB to the lowest unoccupied molecular orbital (LUMO) of TCNQ. This transition suggests the formation of a transient biradical species, $TMB^{+\bullet} - \pi - TCNQ^{-\bullet}$, with evidence from Raman spectra. Transient absorption spectroscopy indicates that the back-electron-transfer process occurs in about 10 ps.[92] Thanks to the unique capabilities of ultrafast Raman techniques in terms of time and frequency resolutions, through transient absorption and resonance Raman (RR) measurements, it was observed that a low-frequency vibrational mode (peaked at 323 cm^{-1}) is strongly active upon photoexcitation and persists for about 5 ps. This latter should also be involved in the intensity and frequency modulation of a higher frequency mode at 1271 cm^{-1}. The strong anharmonic coupling between these modes potentially results in a conical intersection, allowing nonradiative relaxation to the thermal equilibrium state.

We unravel the relaxation dynamics and quantify the anharmonic coupling between vibrational modes with a specific focus on high- and low-frequency modes. Our approach allows us to validate the hypothesis that vibrational coupling of a few and well-defined modes influences and modulates charge recombination in the GS. We recall here that since Born−Oppenheimer molecular dynamics cannot handle trajectories crossing conical intersections and TD-DFT is not recommended for their static characterization, CIs were not directly investigated.

■ METHODS

The computational approach adopted in this work relies on a protocol developed in recent years, which has proven to be

robust and reliable in the detailed atomistic and molecular level description of various chemically relevant problems, ranging from the reactivity of photoacids in solution[81] to the coupling of solute−solvent vibrational modes in peptide models,[66,71] and vibrational relaxation in noncovalent dimers,[69,70] to mention a few examples. Regarding the description of different computational strategies for nonequilibrium relaxation, we refer the readers to our previous publication for a more exhaustive overview.[93] The calibration of the potential represents the first step to be addressed. For our particular system, some crucial aspects to consider concern the noncovalent nature and the weak interaction forces between the two monomers as well as the CT characteristic of the ES of interest. In this context, methods based on DFT provide a good compromise between accuracy and computational cost for characterizing the GS and ES potential energy surfaces. However, the high conformational freedom of the present case study limits the complete characterization of the PES through the sole use of quantum mechanical methods. The cornerstone tools are ab initio molecular dynamics (AIMD) techniques. Proper sampling of the GS PES allows exploration of the conformational space accessible at room temperature, capturing the natural structural evolution of the two monomers and accounting for their mutual interactions in a more realistic and comprehensive manner. The GS AIMD also provides access to inherently anharmonic vibrational normal modes. As detailed below, a judicious choice of representative points in phase space enables subsequent sampling of the ES PES and the associated vibrational analysis in the Franck−Condon region. The multiresolution analysis protocol based on wavelet transform localizes signals extracted from AIMD in both time and frequency domains, facilitating vibrational analysis under nonequilibrium conditions. This allows observation of frequency fluctuations over time, considering anharmonicity and vibrational couplings, providing a valuable tool for comparison with modern time-resolved spectroscopic techniques. We wish to mention here that there have been several attempts to extend AIMD-based approaches to enable some time resolution in the vibrational analysis of nonequilibrium-photoinduced relaxation by, for example, using short-time Fourier transform combined with generalized[94,95] or by directly defining the instantaneous[96−99] normal modes. Although, instantaneous normal modes and short-time FT-based methods are usually valid, sometimes they can suffer from the fixed frequency−time resolution, while wavelet transform can provide an intrinsic multiresolution approach.[71]

The molecular dynamics trajectories for the S_0 and S_1 electronic states were analyzed in terms of a detailed structural analysis to quantify the effect on each molecular subunit of the electronic density reorganization upon excitation followed by a time-resolved vibrational analysis by focusing the attention on two vibrational modes mainly localized on the TCNQ acceptor monomer. In the latter case, the theoretical strategy exploited in this work has been already presented in detail elsewhere by some of the authors.[69,71,81,100] Here, we briefly give a resume: at any temperature, the generalized normal-like modes correspond on average to the uncorrelated momenta of atom groups.[100,101] Through ab initio molecular dynamics trajectories, generalized normal modes can be extracted, and their power spectra (comparable to IR and Raman profiles) can be computed by means of the Fourier transform.[102−104] For each step of the trajectory, rotational modes of the system were projected out by a minimization procedure of the angular momentum with respect to the orientation assumed by the molecule in the first time step. In this work, concerning the GS trajectory, this procedure was applied only for coordinates and momenta of TCNQ rather than for the entire complex since in this way, an improved description (less noisy spectra and smoother peaks) of the vibrational mode composition and relative spectra was achieved. The generalized normal modes are computed by the transformation matrix, $\mathbf{L}$, which diagonalizes the covariance matrix of the mass weighted atomic velocities, $\mathbf{K}$, with elements

$$K_{ij} = \frac{\sqrt{m_i m_j}}{2} \langle (\dot{x}_i - \langle \dot{x}_i \rangle)(\dot{x}_j - \langle \dot{x}_j \rangle) \rangle \tag{1}$$

Indexes i and j run over the $3N$ atomic Cartesian coordinates and m_i represents the mass associated with the corresponding Cartesian velocity, $\dot{x}_j$, collected along the trajectory. The quantity reported in $\langle \rangle$ represents the ensemble average constructed in this work by averaging over the time. The normal modes have been obtained as eigenvectors of $\mathbf{K}$, while eigenvalues of $\mathbf{K}$ provide averaged kinetic energy for each mode.

An extension to characterize the generalized normal mode in the Franck−Condon region and their relaxation dynamics of such procedure was recently presented by some of the authors in ref 81. According to this protocol, one or more ES MD trajectories are collected first, and then we assume that the normal mode compositions are unchanged with respect to the GS. This approximation holds in the ultrafast regime of the relaxation process allowing to project the ES atomic velocities of the TCNQ and TMB subunits along GS generalized normal mode vectors to obtain their evolution in the Franck−Condon region. Generalized mode velocities $\dot{\mathbf{Q}}$ for the corresponding electronic state of interest are calculated at each time step by projecting either GS or ES atomic velocities along generalized normal modes

$$\dot{\mathbf{Q}}_{GS/ES}(t) = \mathbf{L}^{\dagger} \dot{\mathbf{x}}_{GS/ES}(t) \tag{2}$$

where $\mathbf{L}$ is the unitary transformation which diagonalizes $\mathbf{K}$ and is assumed fixed for both electronic states. Generalized normal mode velocity power spectrum $P^{\alpha}(\omega)$ for a given normal mode can be directly computed via the Fourier transform of its autocorrelation function[105] according to the following expression

$$P^{\alpha}(\omega) = \int \langle \dot{Q}_{GS/ES}^{\alpha}(\tau) \dot{Q}_{GS/ES}^{\alpha}(t + \tau) \rangle_{\tau} e^{-i\omega t} dt \tag{3}$$

where α runs over the $3N$ generalized normal coordinates, 3 related to translational motions and the other 3 to rotational collective motions, respectively. Results from ES molecular dynamics are presented as an average of three trajectories.

To interpret, at the molecular level, the time evolution of a spectroscopic signal around the Franck−Condon region, a time-resolved vibrational protocol based on the continuous wavelet transform (cWT),[79,80] is here employed. The wavelet protocol is particularly advantageous compared to other signal processing techniques (consider for example the Fourier transform or its short-time variant) as it allows for analyzing frequencies at different resolutions, known as multiresolution analysis, while preserving the information relating to the time domain as well as to the frequency domain. Considering a given time-dependent data set $D(t)$, cWT acts on it according to $W(a, b) = \int D(t) \psi_{a,b}(t) dt$, where the ψ function, called the

wavelet mother function, is normalized and has this mathematical expression: $\psi_{a,b}(t) = |a|^{-1/2}\left(\frac{t-b}{a}\right)$ ($a, b \in \mathbb{R}$, $a > 0$). The wavelet represents the basis function and acts as a window function for the signal processing. It is possible to change the width of the wavelet function and its central frequency along the entire time-dependent signal by changing parameter a, proportional to the inverse of frequency, named the scaling factor. It follows that an expanded wavelet, with a large value of a, solves better for low-frequency components of the signal, however, at the expense of the time resolution. On the contrary, a low value of the scaling parameter, a, shrinks the wavelet function, resulting in a better resolution for high-frequency components and time resolution. Also, b is the translation parameter and shifts the set of all dilated or compressed wavelet functions along the time axis. On the basis of previous works,[106−109] we have agreed to use the Morlet wavelet as mother function[110] as due to the nature of the signals extracted from the AIMD simulations, it provides good accuracy in time and frequency resolutions.

Initial Points in the Phase Space to Sample the Franck−Condon Region. The choice of the initial conditions to sample the ES potential energy surface represents a crucial point to take into account for a reliable characterization of the nuclear relaxation dynamics near the Franck−Condon region.[93] Given the noncovalent nature of the case study, from a geometrical point of view, a natural choice can be well represented by the distance between the two subunits together with specific electronic features. In this regard, we analyzed the time evolution of the center of mass distances between the donor and acceptor moieties explored in the GS (Figure S1 panel A). Such a geometric parameter increases slightly after 2 ps of simulation and oscillates around 4.00 Å, on average. To have an additional insight about the relative distance between the two monomers, we computed the distance distribution function (reported in panel B of Figure S1) for which the maximum peak is within 3.800−4.250 Å close to the average value of 3.983 Å with fluctuations that demonstrate a certain degree of flatness of the GS PES along the TMB $\leftrightarrow$ TCNQ coordinate. From the GS phase space sampling, we selected three points as starting configurations and momenta of as many ES molecular dynamics simulations. The starting points were picked up to reproduce some crucial structural and electronic characteristics such as (i) C.o.M. distances representative of the GS sampling (reported as color bars in panel C of Figure S1), (ii) the total GS and first singlet ES natural bond orbital (NBO) charges, and finally (iii) the values of vertical excitation energies for the $S_1 \leftarrow S_0$ and $S_2 \leftarrow S_0$ electronic transitions. The starting geometries including such parameters are sketched in Figure S2, and a detailed discussion concerning the C.o.M. time evolution is provided below.

Computational Details. In this section, we illustrate the computational details related to static and ab initio molecular dynamics (AIMD) calculations. Concerning the static approach, the optimization calculations without any constraints, energies, harmonic, anharmonic frequencies, and IR intensities were performed on the S_0 and S_1 PESs in the gas phase starting from at least two molecular guesses. The GS electronic structures were obtained by solving the Kohn−Sham equation using the hybrid Becke three-parameter Lee−Yang−Parr (B3LYP) density functional[111−113] and the Coulomb-

attenuating approach (CAM-B3LYP)[114] for ESs in its time-dependent approach. The long-range corrected Coulomb attenuated hybrid functional class[114−118] has been shown to predict CT and Rydberg-like excitation energies/bands more accurately due to their high sensitivity to the treatment of exact exchange[119−131] with respect to the hybrid density functionals (i.e., B3LYP and Perdew−Burke−Ernzerhof-0[132,133]). Weak interactions between monomers have been described correcting potentials with Grimme dispersion (GD3).[134−139] Since no vibrational couplings with the vibrational modes of solvent are expected, we did not account for solvation in our investigation; furthermore, due to the low dielectric constant of DCM (ϵ = 8.93), the effects on geometry, vertical excitations, and so on were negligible (data not reported). By exploiting the atom-centered density matrix propagation (ADMP) formalism,[72−76] we collected a 10 ps-long GS ab initio molecular dynamics trajectory after 1 ps of equilibration with a time step of 0.2 fs at the B3LYP/6-31G(d,p)/GD3 theory level. A temperature of 300 K was enforced by rescaling the nuclear velocities each 1 ps. One of the equilibrium geometries (the less stable one) has been chosen as the starting point. We performed TD-DFT single-point calculations on several geometries randomly extracted from the GS sampling, comparing the performances of two different basis sets (6-31G(d,p) and 6-31+G(d,p)) for checking the accuracy of the smaller basis set. The vertical excitation energy (VEE), oscillator strength, and largest molecular orbital coefficients are presented, for 13 geometries, in Tables S1 and S2, and no significant changes are present. Comparing the values obtained with two different basis sets, it is possible to evaluate that the presence of diffuse functions on heavy atoms induces only a slight red shift of the excitation energies with a maximum discrepancy calculated equal to 0.04 eV.

ES ab initio molecular dynamics simulations, according to the Born−Oppenheimer (BOMD) propagation scheme,[77,78] have been sampled at the CAM-B3LYP/6-31G(d,p)/GD3 theory level for about 7.5 ps simulation time, with a time step of 0.7 fs starting from three coordinates and momenta sets chosen from GS-AIMD. All ab initio calculations have been performed by using the GAUSSIAN suite program.[140] In this paper, the signals processed by cWT ($D(t)$ in the expression above) are the $\dot{Q}^\alpha_{GS/ES}$ extracted from the GS or first singlet ES AIMD trajectory, this latter considered as an average over the ES trajectories. The cWT time-resolved vibrational power spectra are plotted as a perspective map for ease of reading. The frequency is reported on the y-axis in cm^{-1}, the time is expressed in fs on the x-axis, and the color scale on the z-axis represents the magnitude, $|W(v,t)|^2$, of the power spectrum. The frequency values discussed below were identified by considering the main signal with the maximum magnitude in the power spectrum. The resolution in the frequency domain ranges from ∼5 cm^{-1} for the CCN bending mode in the low-energy part of the spectrum (below 500 cm^{-1}) to ∼25 cm^{-1} for the CC rocking mode at energies above 1000 cm^{-1}.

■ RESULTS AND DISCUSSION

Structural Characterization by Static and Dynamical Approaches. The potential energy surface of the loosely bound complexes is relatively flat, and numerous equilibrium conformers are expected to be present very close in energy. In our study, we explored several relative arrangements of the two monomers (refer to Figures S3 and S4 in the Supporting

Information). Our focus centered on analyzing the lower-energy π-stacked minima, while those at higher energy, leading to dark electronic transitions, as documented in Table S3 in the Supporting Information, were not further studied. Two minimum energy structures (see Figure 2) have been
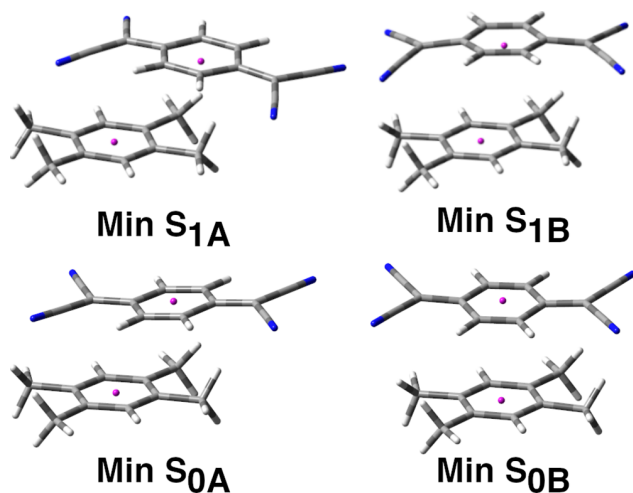

Figure 2. Representative GS minimum energy structures named $MinS_{0A,B}$ from bottom left to right, respectively, computed in the gas phase at the B3LYP/6-31+G(d,p)/GD3 theory level. First singlet ES energy minima, from top left to right, computed in the gas phase at the CAM-B3LYP/6-31+G(d,p)/GD3 level named $MinS_{1A,B}$, respectively. The center of mass of each monomer is represented as a purple sphere.

considered for the fundamental electronic state starting from different geometrical guesses under vacuum and in solvent (DCM) that differ negligibly in energy (ΔE_{vacuum} = 1.03 kcal/mol and ΔE_{DCM} = 0.99 kcal/mol). The most stable TMB:π:TCNQ complex, named $MinS_{0A}$, is a π-stacked structure in which the two rings are not exactly coplanar and are placed at a distance of the center of mass (C.o.M) of 3.99 Å. On the contrary, the $MinS_{0B}$ geometry shows that the two monomers retain the face-to-face arrangement, and the two rings are more overlapped for which the distance between the center of mass is 0.58 Å less than the previous case.

Both GS minima have been considered as starting points for geometry optimization in the first singlet ES (top panel of Figure 2). Upon photoexcitation, the equilibrium structure relaxes and adapts its geometry toward a structural arrangement consistent with the new electron density. We found that the energy differences are similar in magnitude to the GS case, but the $MinS_{1B}$, for which the two monomers are at 3.48 Å, turns out to be more stable (ΔE = 0.96 kcal/mol). The TCNQ monomer in $MinS_{1A}$ appears to be more significantly displaced from the donor monomer, TMB. Therefore, the distance between the centers of mass is calculated to be 4.43 Å. For this latter, the acceptor monomer adopts a visible distorted boat shape, bended toward the TMB molecule. The difference of the bond lengths calculated in both electronic states for the two minima considered are reported in ESI under Figure S5. It can be summarized that the TCNQ acceptor monomer passes from a typically quinoid structure to a benzenoid-like one.[87,89] The TMB donor monomer (Figure S5, bottom), yielding electronic density due to excitation, undergoes mainly structural changes involving the aromatic ring that rearranges significantly toward an quinoidal structure.

We analyzed the nature of electronic transitions in terms of molecular orbital compositions by performing time-dependent DFT calculations simulating the optical absorption spectrum of the TMB:π:TCNQ-isolated CT complex. TD-DFT calculation predicts that the $S_1 \leftarrow S_0$ transition is purely a HOMO–LUMO transition at 542 nm (2.29 eV, f = 0.184) for the most stable conformer ($MinS_{0A}$) and 573 nm (2.16 eV, f = 0.047) for the second one, both centered within the experimental UV–vis long wavelength band recorded in DCM solution. Frontier molecular orbitals, HOMO and LUMO, reported in Figure 3 are located on donor and acceptor monomers,
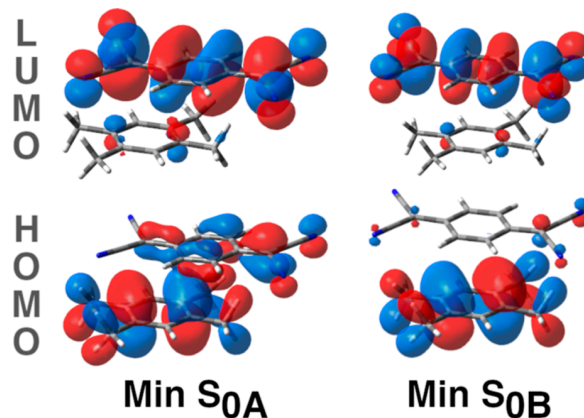

Figure 3. HOMO and LUMO molecular frontier orbitals (isovalue = 0.02) involved in the $S_1 \leftarrow S_0$ electronic transition computed in the gas phase at CAM-B3LYP/6-31+G(d,p)/GD3 for the two minima $MinS_{0A,B}$, from left to right, respectively.

respectively, implying that the first singlet ES exhibits a clear CT characteristic. Although MO isosurfaces are very informative, we performed a natural bond order population analysis to have quantitative insights on the electronic rearrangement of the TMB:π:TCNQ complex upon photoexcitation. In the GS, we find a discrete charge separation for both molecular complexes: $\pm 0.128e$ for $MinS_{0A}$ and $\pm 0.095e$ for $MinS_{0B}$ (the minus sign it refers to the TCNQ molecule) that rules the weak interactions between the two monomers and allows the formation of π-stacked dimers. In the ES, the charge distribution changes drastically, and we find, for both minima, a charge separation close to $1e$ ($MinS_{1A} \pm 0.948e$ and $MinS_{1B} \pm 0.949e$), suggesting the formation of a biradical species in which the TCNQ received an electron ($TCNQ^{-\bullet}$) from the donor monomer ($TMB \rightarrow TMB^{+\bullet} + 1e^-$). These trends are in agreement with the experimental hypothesis.[91] The results shown here exemplify the main role of the photoexcitation on this noncovalent intermolecular CT dimer.

The vibrational analysis, in the harmonic approximation, was mainly focused toward the identification of the two normal modes: the in-plane CCN bending and the CC rocking mode associated with the TCNQ monomer, which are supposed to be the driving force of the ES reactivity due to the anharmonic coupling between them.[91] The composition of normal modes computed in the GS and first singlet ES is depicted in Figure 4 for $MinS_{0B}$, as an example. The whole vibrational spectra of the TMB:π:TCNQ EDA complex computed in the gas phase on the S_0 and S_1 electronic states are shown in Figure S6 in the Supporting Information.

In the same fashion, we also provide a comprehensive and quantitative analysis of various structural parameters of the CT
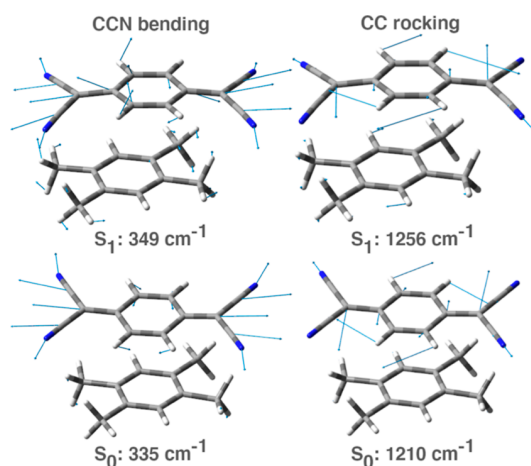
Figure 4. Composition of vibrational modes of interest, calculated for the S_0 (bottom) and S_1 (top) electronic states. The in-plane CCN bending mode (left) and the CC rocking mode are mainly localized on the TCNQ acceptor and both undergo a blue shift of frequency when in ES of about 15 and 45 cm^{-1}, respectively.

complex performed this time by GS and ES AIMD trajectories taking into account bond lengths, bond angles, and dihedrals. The normal distributions of selected bond lengths of the single TCNQ (Figures S7 and S8) and TMB (Figure S9) molecules have highlighted the greatest structural differences passing from the GS to the ES PESs. The main structural changes found mostly concern the double bonds inside the acceptor ring (C_1–C_2 and C_4–C_5) and similarly for C_6–C_7 and C_3–C_{10} that undergo considerable lengthening following the photo-

excitation. In particular, the ring double bonds increase by 0.011 Å on average and 0.03 Å for those outside the ring which undergo the maximum elongation. Single CC bonds go in the opposite direction; this is particularly evident for the CC bonds of the ring that change more (0.02 Å) due to the new electronic distribution. The triple bond of the cyano groups is shortened in a negligible way (0.001 Å) The effects due to the photon absorption are summarized here for the donor monomer. The double bonds of the ring adjacent to the methyl group undergo the maximum elongation (0.05 Å on average), while the methyl groups approach to the aromatic ring (0.025 Å) as the remaining CC bonds (0.02 Å). It can therefore be guessed that the electronic density is spread over all double bonds of the acceptor, and the entire molecule is stretched in the C_7–C_{10} direction. The six-membered ring of the donor, on the contrary, is now stretched along the C_3–C_6 axes. The same considerations are reached through the study of the frontier molecular orbitals most involved in the electronic transition (reported in Figure 3). Furthermore, we observe good agreement between the structural analysis performed on equilibrium geometries and from the AIMD trajectories. Bond lengths, bond angles, and dihedral angles are tabulated and reported in Tables S4 and S5 in the Supporting Information.

From the visual inspection of the AIMD trajectories sampled in the GS and the first singlet ES with CT characteristic, we observed that the π–π stacked arrangement of the two monomers is favored over other typical topologies such as T-shaped, parallel displaced, and edge to face that have never been found. We computed the distance between the centers of mass of the two monomers (see panels A of Figures S1 and
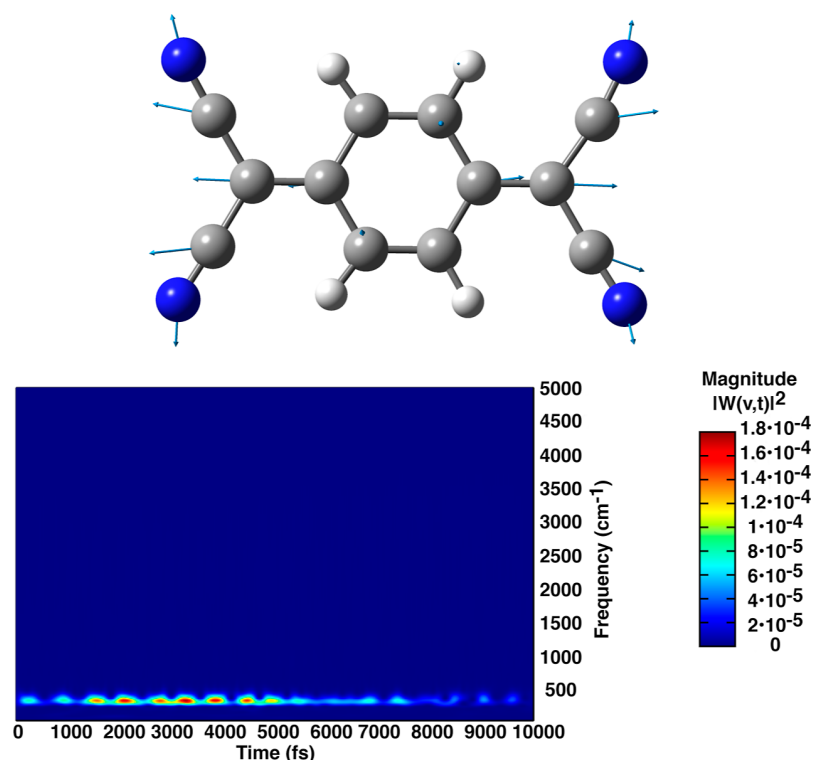

Figure 5. In-plane CCN bending generalized normal mode composition (top) localized on the TCNQ acceptor subunit along with the time-resolved wavelet spectrum (bottom) shown in perspective view. The magnitude $|W(\nu,t)|^2$ of the power spectrum is reported as a color scale on the right.
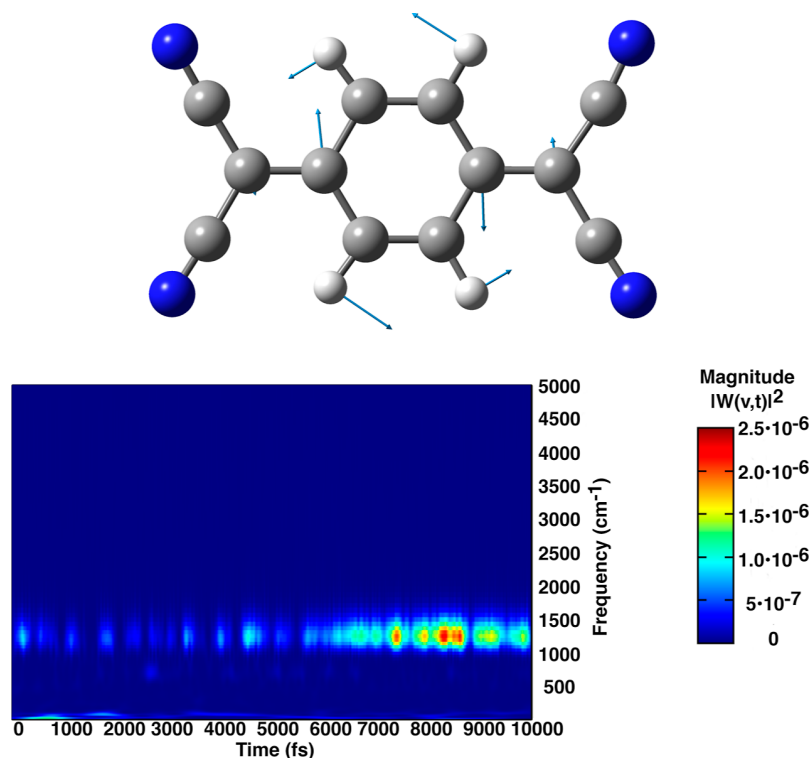
Figure 6. CC rocking generalized normal mode composition (top) localized on the TCNQ acceptor subunit along with the time-resolved wavelet spectrum (bottom) shown in perspective view. The magnitude $|W(\nu,t)|^2$ of the power spectrum is reported as a color scale on the right.

S10−S12 in the Supporting Information) for each trajectory: for the 10 ps long GS one (**trj S_0** in Figure S1), the two monomers are at an average distance of 3.983 Å reaching the maximum distance of 4.522 Å at $\simeq$3.5 ps. The closest point of contact occurs in 1.5 ps (3.336 Å). Two ES trajectories showed a similar behavior (**trj I S_1** in Figure S10 and **trj II S_1** in Figure S11); on average, the distance between the two subunits is 3.810 and 3.765 Å, respectively. Due to the new electron distribution following the photoexcitation and the formation of a biradical species, the CT complex is able to reach a minimum distance of $\simeq$0.4 Å below that observed for the GS. The last ES trajectory (**trj III S_1** in Figure S12) shows a visibly different trend with maximum just above $\sim$6 Å within the first 3 ps, then decreases to 2.980 Å (minimum distance), and then increase again around $\sim$5 Å. The apparently discordant trend with the ES minimum energy geometries discussed above was verified by carefully analyzing the frames of this trajectory: at distances close to $\sim$6 Å, the TCNQ monomer slipped with respect to the donor monomer, superimposing a single region of the molecule (NCCCN) on the TMB ring. For these geometric implications, the distance between the centers of mass assumes greater values than those observed for the other two trajectories.

Vibrational Dynamics from Ab Initio Molecular Dynamics Simulations. In this section, our main focus concerns the vibrational analysis of two generalized normal modes of interest extracted from the GS and the averaged ES AIMD trajectories relying on the protocol reported in the Methods section.

The in-plane CCN bending mode extracted from the GS AIMD trajectory taking into account only the coordinates and momenta of the acceptor monomer (thus to obtain a less crowded and more resolved spectrum) is completely localized on the TCNQ acceptor (Figure 5, top). Interestingly, the composition of the normal mode is very similar to that canonically obtained by the Hessian matrix diagonalization discussed in Figure 4. The time-independent vibrational spectrum, reported in Figure S13 in the Supporting Information, shows two well-defined and isolated features in the low-energy region. The main one is peaked at 334 cm^{-1} and represents the frequency of interest, while the less intense at 380 cm^{-1} can be ascribed, with the help of Hessian-based vibrational analysis, to another TCNQ bending mode with a slightly similar composition. The wavelet spectrum shows a well-resolved band centered below 500 cm^{-1} and exactly at 330 cm^{-1} in agreement with Hessian-based harmonic calculation, whose magnitude is exhausted starting from about 6.5 ps. In the same way, we extracted the CC rocking mode which is depicted in Figure 6, also in this case similar in composition to that obtained from the calculation of vibrational modes on the GS minimum. In the related Fourier spectrum (see Figure S14 in the Supporting Information), a feature peaked at an anharmonic frequency of 1287 cm^{-1} is present, and no other important signals are detected. The associated magnitude in the time-resolved power spectrum begins to rise from 6.5 ps and persists for the rest of the sampled time. Available spectroscopic data in the literature, at the best of our knowledge, do not report about frequency values for this specific noncovalent system in the ground electronic state; hence, a direct comparison between our time-resolved vibrational dynamics with experimental findings is not possible.

The vibrational dynamics of the TMB:π:TCNQ complex has been investigated on the first singlet ES PES in which the charge separation confers a biradical nature. Also in this case, our focus will be the characterization of the vibrational modes mainly involved in the photorelaxation downhill the Franck−
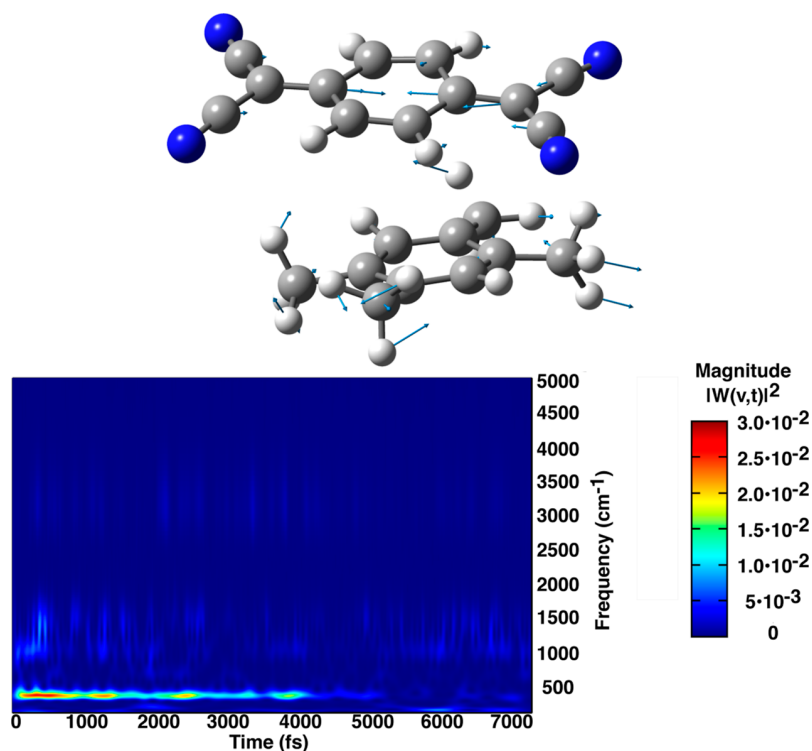
Figure 7. In-plane CCN bending generalized normal mode composition (top) extracted from the average of three ES trajectories along with the time-resolved wavelet spectrum (bottom) shown in perspective view. The magnitude $|W(v,t)|^2$ of the power spectrum is reported as a color scale on the right.
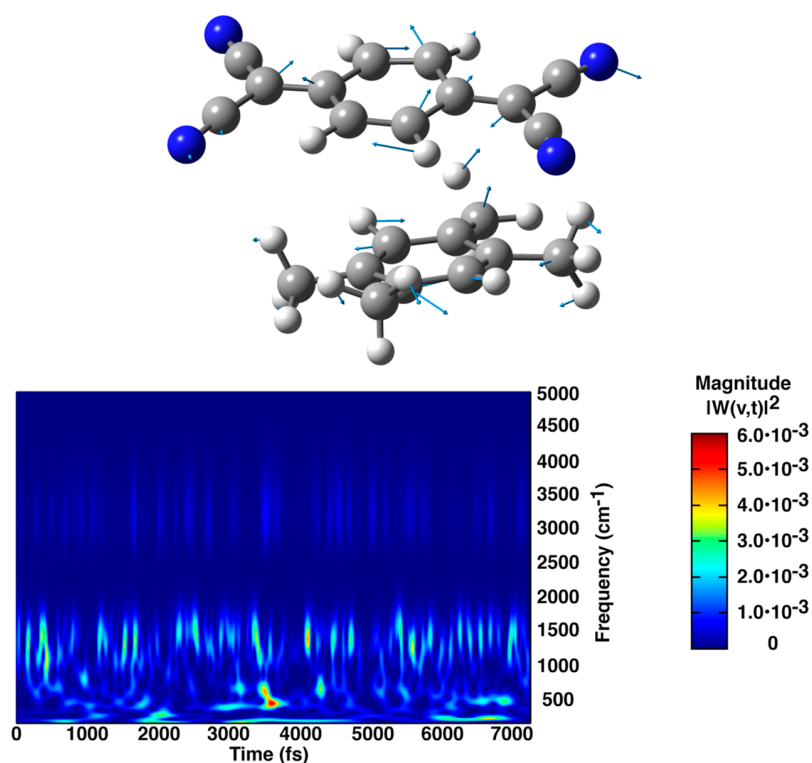

Figure 8. CC rocking generalized normal mode composition (top) extracted from the average of three ES trajectories along with the time-resolved wavelet spectrum (bottom) shown in perspective view. The magnitude $|W(v,t)|^2$ of the power spectrum is reported as a color scale on the right.

Condon region. Inspecting the static vibrational spectrum reported in Figure S15 in the Supporting Information, several vibrational features are present, namely, due to the contribution of vibrational modes of the TMB donor monomer around 1000, 1500, and above 3000 cm^{-1}, in addition to the most important one peaked at 352 cm^{-1}. It is also observed
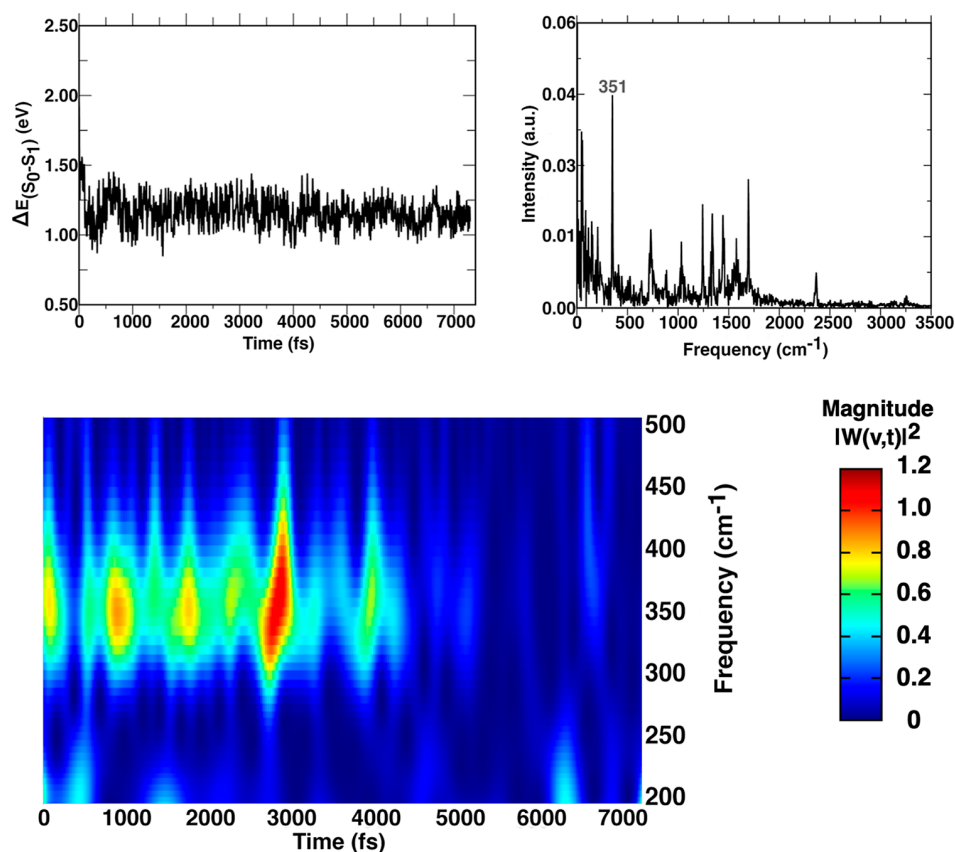
Figure 9. Time evolution of the S_0–S_1 electronic energy separation (eV, top left) as an average of three ES trajectories and the time-independent vibrational spectrum that shows a main peak at 351 cm^{-1} (top right). The time-resolved vibrational spectrum (bottom) highlights a signal around 350 cm^{-1} which lasts for ~5 ps.

that the vibrational mode in Figure 7 is recognizable, although it is inherently more complex than the previous case. The wavelet spectrum in Figure 7 shows that the band around 350 cm^{-1} is the main feature and that other signals observed in the FT spectrum do not contribute significantly. Another important observation regards the time evolution of the magnitude of the signal: in the FSRS experiments, the TCNQ CCN bending mode persists for $\simeq$5 ps upon the electronic excitation, and accordingly, our time-resolved vibrational spectrum shows that the magnitude of the CCN mode decreases gradually within the same time scale. This interesting trend in agreement with experimental counterparts was always observed for all the three sampled trajectories. The maximum magnitude of the main band versus time, reported for completeness in Figure S16 in the Supporting Information, clearly highlights the activation lifetime of the CCN bending mode.

At higher energies, the CC rocking mode of the TCNQ acceptor is present. The composition of the normal mode is shown at the top of Figure 8. The Fourier spectrum (Figure S17) is more crowded, and several signals in addition to the main one centered at 1260 cm^{-1} are present. As stated in a work recently published by some of the authors,[69] the wavelet analysis applied to $\dot{\mathbf{Q}}$ is extremely informative; indeed, from the temporal evolution of a vibrational band, the quantification of the anharmonic coupling between modes that occur on the ES PES is easily accessible. By inspecting the time-resolved wavelet spectrum in Figure 8, in addition to the main band which shows a clear oscillatory behavior over time, the

presence of other minor components is observed. 2D-FSRS gave an additional insight into the mode−mode coupling, revealing that the 1271 cm^{-1} CC rocking mode is strongly anharmonically coupled to the 323 cm^{-1} CCN bending and the 354 cm^{-1} TMB out-of-plane deformation modes and also a detectable coupling to the 105 or 151 cm^{-1} modes, both of which involve deformation of the CCN angle. In order to extrapolate detailed information about the observed frequency modulations, we extracted the magnitude over time of the signal centered at 1260 cm^{-1} (see Figure S18, top panel). Interestingly, Fourier transforms of the frequency magnitude fluctuations of the CC rocking mode, a clear feature at 360 cm^{-1}, attributable to the TCNQ CCN bending (Figure S18, bottom panel), can be observed along with several other low frequencies related to large amplitude modes as collective dimer modes and ring deformations (less than 300 cm^{-1}).

We provide here in Figure 9 a further analysis that allowed us to identify the tuning vibrational mode for the CI that governs and controls the charge recombination internal conversion. The vibrational analysis has been carried out on the time evolution of the S_0–S_1 energy gap as an average of the three sampled trajectories. From the Fourier transform spectrum, a main peak at 351 cm^{-1} can be recognized; in the time-resolved vibrational spectrum, a signal is present again within the first 5 ps. This result confirms that actually the CCN bending acts as the tuning mode modulating the energy gap between the S_0 and S_1 CT electronic states.

■ CONCLUSIONS

In this study, we investigated a noncovalent $\pi-\pi$ stacked dimer using quantum mechanical and dynamic approaches within the frameworks of DFT and time-dependent DFT. We explored both the GS and the first singlet ES, with a particular focus on the strong charge separation that occurs upon excitation.

Initially, we performed a quantum mechanical examination of representative equilibrium structures to evaluate the accuracy of our methods and the modeling approach. This evaluation included a comparison of the infrared and electronic absorption spectra to their experimental counterparts. Our primary objectives were to characterize the potential energy surfaces and finely assess the interplay between electronic and structural properties following photoexcitation in the low-lying ES. We also aimed to uncover the vibrational relaxation process within the Franck−Condon region, which could act as precursor steps leading to the nonadiabatic dynamics of the photorelaxation from the CT state to the GS.

One of the most notable macroscopic effects observed after electronic excitation was the convergence of the two subunits, driven by the increased Coulombic attraction resulting from CT from TMB to TCNQ. Additionally, the TCNQ, which initially exhibited a quinoid structure, transitioned to a benzenoid-like arrangement, while the TMB, an electron donor, experienced the opposite transformation.

The core of our work relied on a recently proposed computational protocol that involved the analysis of generalized normal modes extracted from adiabatic ab initio molecular dynamics simulations in both the GS and CT electronic states. This approach allowed us to obtain time-resolved vibrational spectra through the wavelet transform of specific quantities.

Our findings were in good agreement with experimental expectations. Two vibrational modes in the ES, specifically the CCN bending mode at 352 cm^{-1} and the CC rocking mode centered at 1271 cm^{-1}, were found to play a crucial role in the relaxation dynamics of the TMB:π:TCNQ molecular complex. Moreover, we quantified the anharmonic coupling between the CC rocking and CCN bending modes on the TCNQ acceptor monomer, confirming experimental assumptions.

Importantly, our protocol allowed us to identify the vibrational mode responsible for modulating the energy separation between the S_0 and S_1 states. The CCN bending mode emerged as the key tuning mode, potentially driving the system into a nonadiabatic region and completing the photorelaxation process of the entire TMB:π:TCNQ complex back to the GS.

■ ASSOCIATED CONTENT

ⓈⒾ Supporting Information

The Supporting Information is available free of charge at https://pubs.acs.org/doi/10.1021/acs.jpca.3c08366.

> TD-DFT single-point calculations performed on geometry randomly extracted from the GS-AIMD trajectory; temporal evolution and normalized distribution of the center of the mass distance computed from the GS AIMD trajectory; TMB:π:TCNQ initial geometries to run ES BOMD simulations; TMB:π:TCNQ structural isomers computed in the GS at the B3LYP/6-31+G-(d,p)/GD3 theory level; TD-DFT single-point calculations performed on several TMB:π:TCNQ structural isomers at the CAM-B3LYP/6-31+G(d,p) theory level;

comparison of bond length variations computed for TMB:π:TCNQ S_0 and S_1 optimized structures; comparison of infrared spectra computed in the GS and first singlet ES; average structural parameters extracted from S_0 and S_1 AIMD trajectories for TCNQ and TMB monomers; normalized distributions of relevant structural parameters for TCNQ and TMB monomers computed from S_0 and S_1 AIMD trajectories; comparison of the temporal evolution of the center of the mass distance computed from the GS and first singlet ES AIMD trajectories; temporal evolution and normalized distribution of the center of the mass distance computed from each ES AIMD trajectory; Fourier spectrum of the CCN bending mode computed from the GS AIMD trajectory; Fourier spectrum of the CC rocking mode computed from the GS AIMD trajectory; Fourier spectrum of the CCN bending mode computed from the ES AIMD trajectory; magnitude fluctuations over time for the CCN bending mode extracted from ES wavelet analysis; Fourier spectrum of the CC rocking mode computed from the ES AIMD trajectory; magnitude fluctuations over time for the CC rocking mode extracted from ES wavelet analysis and its Fourier spectrum (PDF)

■ AUTHOR INFORMATION

Corresponding Author

Nadia Rega − *Department of Chemical Sciences, University of Napoli Federico II, Complesso Universitario di M.S. Angelo, 80126 Napoli, Italy; Scuola Superiore Meridionale, I-80138 Napoli, Italy; Istituto Nazionale Di Fisica Nucleare, sezione di Napoli, Complesso Universitario di Monte S. Angelo ed. 6, 80126 Napoli, Italia;* ⓘ orcid.org/0000-0002-2983-766X; Email: nadia.rega@unina.it

Authors

Federico Coppola − *Scuola Superiore Meridionale, I-80138 Napoli, Italy;* ⓘ orcid.org/0000-0002-5845-4211

Paola Cimino − *Department of Chemical Sciences, University of Napoli Federico II, Complesso Universitario di M.S. Angelo, 80126 Napoli, Italy*

Alessio Petrone − *Department of Chemical Sciences, University of Napoli Federico II, Complesso Universitario di M.S. Angelo, 80126 Napoli, Italy; Scuola Superiore Meridionale, I-80138 Napoli, Italy; Istituto Nazionale Di Fisica Nucleare, sezione di Napoli, Complesso Universitario di Monte S. Angelo ed. 6, 80126 Napoli, Italia;* ⓘ orcid.org/0000-0003-2232-9934

Complete contact information is available at:
https://pubs.acs.org/10.1021/acs.jpca.3c08366

Notes

The authors declare no competing financial interest.

■ ACKNOWLEDGMENTS

■ REFERENCES

(1) Kuznetsov, A. M. *Charge transfer in physics, chemistry and biology: physical mechanisms of elementary processes and an introduction to the theory*; CRC Press, 2020.

(2) May, V.; Kühn, O. *Charge and energy transfer dynamics in molecular systems*; John Wiley & Sons, 2008.

(3) Biskup, T.; Hitomi, K.; Getzoff, E. D.; Krapf, S.; Koslowski, T.; Schleicher, E.; Weber, S. Unexpected Electron Transfer in Cryptochrome Identified by Time-Resolved EPR Spectroscopy. *Angew. Chem., Int. Ed.* **2011**, *50*, 12647−12651.

(4) Koslowski, T.; Burggraf, F.; Krapf, S.; Steinbrecher, T.; Wittekindt, C. Recent progress in biological charge transfer: Theory and simulation. *Biochim. Biophys. Acta, Bioenerg.* **2012**, *1817*, 1955−1957.

(5) Yaroshevich, I. A.; Maksimov, E. G.; Sluchanko, N. N.; Zlenko, D. V.; Stepanov, A. V.; Slutskaya, E. A.; Slonimskiy, Y. B.; Botnarevskii, V. S.; Remeeva, A.; Gushchin, I.; et al. Role of hydrogen bond alternation and charge transfer states in photoactivation of the Orange Carotenoid Protein. *Commun. Biol.* **2021**, *4*, 539.

(6) Sasaki, S.; Drummen, G. P.; Konishi, G.-i. Recent advances in twisted intramolecular charge transfer (TICT) fluorescence and related phenomena in materials chemistry. *J. Mater. Chem. C* **2016**, *4*, 2731−2743.

(7) Srimuk, P.; Su, X.; Yoon, J.; Aurbach, D.; Presser, V. Charge-transfer materials for electrochemical water desalination, ion separation and the recovery of elements. *Nat. Rev. Mater.* **2020**, *5*, 517−538.

(8) Domcke, W.; Yarkony, D.; Köppel, H. *Conical intersections: electronic structure, dynamics & spectroscopy*; World Scientific, 2004; Vol. *15*.

(9) Domcke, W.; Yarkony, D. R.; Köppel, H. *Conical intersections: theory, computation and experiment*; World Scientific, 2011; Vol. *17*.

(10) Hamm, P.; Stock, G. Vibrational conical intersections as a mechanism of ultrafast vibrational relaxation. *Phys. Rev. Lett.* **2012**, *109*, 173201.

(11) Domcke, W.; Yarkony, D. R. Role of conical intersections in molecular spectroscopy and photoinduced chemical dynamics. *Annu. Rev. Phys. Chem.* **2012**, *63*, 325−352.

(12) Kowalewski, M.; Fingerhut, B. P.; Dorfman, K. E.; Bennett, K.; Mukamel, S. Simulating coherent multidimensional spectroscopy of nonadiabatic molecular processes: From the infrared to the x-ray regime. *Chem. Rev.* **2017**, *117*, 12165−12226.

(13) Hall, C. R.; Conyard, J.; Heisler, I. A.; Jones, G.; Frost, J.; Browne, W. R.; Feringa, B. L.; Meech, S. R. Ultrafast dynamics in light-driven molecular rotary motors probed by femtosecond stimulated Raman spectroscopy. *J. Am. Chem. Soc.* **2017**, *139*, 7408−7414.

(14) Ikeda, T.; Tanimura, Y. Probing photoisomerization processes by means of multi-dimensional electronic spectroscopy: The multi-state quantum hierarchical Fokker-Planck equation approach. *J. Phys. Chem. A* **2017**, *147*, 014102.

(15) Duan, H.-G.; Qi, D.-L.; Sun, Z.-R.; Miller, R. D.; Thorwart, M. Signature of the geometric phase in the wave packet dynamics on hypersurfaces. *Chem. Phys.* **2018**, *515*, 21−27.

(16) Oliver, T. A.; Fleming, G. R. Following Coupled Electronic-Nuclear Motion through Conical Intersections in the Ultrafast Relaxation of β-Apo-8′-carotenal. *J. Phys. Chem. B* **2015**, *119*, 11428−11441.

(17) Liebel, M.; Schnedermann, C.; Kukura, P. Vibrationally coherent crossing and coupling of electronic states during internal conversion in β-carotene. *Phys. Rev. Lett.* **2014**, *112*, 198302.

(18) Satzger, H.; Townsend, D.; Zgierski, M. Z.; Patchkovskii, S.; Ullrich, S.; Stolow, A. Primary processes underlying the photostability of isolated DNA bases: Adenine. *Proc. Natl. Acad. Sci. U.S.A.* **2006**, *103*, 10196−10201.

(19) Hudock, H. R.; Levine, B. G.; Thompson, A. L.; Satzger, H.; Townsend, D.; Gador, N.; Ullrich, S.; Stolow, A.; Martinez, T. J. Ab initio molecular dynamics and time-resolved photoelectron spectroscopy of electronically excited uracil and thymine. *J. Phys. Chem. A* **2007**, *111*, 8500−8508.

(20) Groenhof, G.; Schäfer, L. V.; Boggio-Pasqua, M.; Goette, M.; Grubmüller, H.; Robb, M. A. Ultrafast deactivation of an excited cytosine- guanine base pair in DNA. *J. Am. Chem. Soc.* **2007**, *129*, 6812−6819.

(21) Wei, Z.; Nakamura, T.; Takeuchi, S.; Tahara, T. Tracking of the nuclear wavepacket motion in cyanine photoisomerization by ultrafast pump−dump−probe spectroscopy. *J. Am. Chem. Soc.* **2011**, *133*, 8205−8210.

(22) Kistler, K. A.; Matsika, S. *Quantum mechanical studies of the photophysics of DNA and RNA Bases*; Multi-scale Quantum Models for Biocatalysis, 2009; pp 285−339.

(23) Kang, H.; Lee, K. T.; Jung, B.; Ko, Y. J.; Kim, S. K. Intrinsic lifetimes of the excited state of DNA and RNA bases. *J. Am. Chem. Soc.* **2002**, *124*, 12958−12959.

(24) Merchan, M.; Gonzalez-Luque, R.; Climent, T.; Serrano-Andres, L.; Rodríguez, E.; Reguero, M.; Pelaez, D. Unified model for the ultrafast decay of pyrimidine nucleobases. *J. Phys. Chem. B* **2006**, *110*, 26471−26476.

(25) Segalina, A.; Francés-Monerris, A.; Pastore, M.; Leininger, T.; Evangelisti, S.; Monari, A. Conical intersection properties unraveled by the position spread tensor. *Theor. Chem. Acc.* **2018**, *137*, 163.

(26) Matsika, S. Radiationless decay of excited states of uracil through conical intersections. *J. Phys. Chem. A* **2004**, *108*, 7584−7590.

(27) Polli, D.; Altoe, P.; Weingart, O.; Spillane, K. M.; Manzoni, C.; Brida, D.; Tomasello, G.; Orlandi, G.; Kukura, P.; Mathies, R. A.; et al. Conical intersection dynamics of the primary photoisomerization event in vision. *Nature* **2010**, *467*, 440−443.

(28) Antol, I. Photodeactivation paths in norbornadiene. *J. Comput. Chem.* **2013**, *34*, 1439−1445.

(29) Musser, A. J.; Liebel, M.; Schnedermann, C.; Wende, T.; Kehoe, T. B.; Rao, A.; Kukura, P. Evidence for conical intersection dynamics mediating ultrafast singlet exciton fission. *Nat. Phys.* **2015**, *11*, 352−357.

(30) Rose, B. D.; Shoer, L. E.; Wasielewski, M. R.; Haley, M. M. Unusually short excited state lifetimes of indenofluorene and fluorenofluorene derivatives result from a conical intersection. *Chem. Phys. Lett.* **2014**, *616−617*, 137−141.

(31) Coppola, F.; Nucci, M.; Marazzi, M.; Rocca, D.; Pastore, M. Norbornadiene/Quadricyclane System in the Spotlight: The Role of Rydberg States and Dynamic Electronic Correlation in a Solar-Thermal Building Block. *ChemPhotoChem* **2023**, *7*, No. e202200214.

(32) Fazzi, D.; Grancini, G.; Maiuri, M.; Brida, D.; Cerullo, G.; Lanzani, G. Ultrafast internal conversion in a low band gap polymer for photovoltaics: experimental and theoretical study. *Phys. Chem. Chem. Phys.* **2012**, *14*, 6367−6374.

(33) De Sio, A.; Camargo, F. V. d. A.; Winte, K.; Sommer, E.; Branchi, F.; Cerullo, G.; Lienau, C. Ultrafast relaxation dynamics in a polymer: fullerene blend for organic photovoltaics probed by two-dimensional electronic spectroscopy. *Eur. Phys. J. B* **2018**, *91*, 236.

(34) Geppert, D.; Seyfarth, L.; de Vivie-Riedle, R. Laser control schemes for molecular switches. *Appl. Phys. B: Lasers Opt.* **2004**, *79*, 987−992.

(35) Cho, M.; Fleming, G. R. Two-Dimensional Electronic−Vibrational Spectroscopy Reveals Cross-Correlation between Solvation Dynamics and Vibrational Spectral Diffusion. *J. Phys. Chem. B* **2020**, *124*, 11222−11235.

(36) Oliver, T. A.; Lewis, N. H.; Fleming, G. R. Correlating the motion of electrons and nuclei with two-dimensional electronic−vibrational spectroscopy. *Proc. Natl. Acad. Sci. U.S.A.* **2014**, *111*, 10061−10066.

(37) Lewis, N. H.; Dong, H.; Oliver, T. A.; Fleming, G. R. Measuring correlated electronic and vibrational spectral dynamics using line shapes in two-dimensional electronic-vibrational spectroscopy. *J. Phys. Chem. A* **2015**, *142*, 174202.

(38) Wu, E. C.; Ge, Q.; Arsenault, E. A.; Lewis, N. H.; Gruenke, N. L.; Head-Gordon, M. J.; Fleming, G. R. Two-dimensional electronic-vibrational spectroscopic study of conical intersection dynamics: an experimental and electronic structure study. *Phys. Chem. Chem. Phys.* **2019**, *21*, 14153−14163.

(39) Kukura, P.; McCamant, D. W.; Mathies, R. A. Femtosecond stimulated Raman spectroscopy. *Annu. Rev. Phys. Chem.* **2007**, *58*, 461−488.

(40) Dietze, D. R.; Mathies, R. A. Femtosecond stimulated Raman spectroscopy. *ChemPhysChem* **2016**, *17*, 1224−1251.

(41) Frontiera, R. R.; Mathies, R. A. Femtosecond stimulated Raman spectroscopy. *Laser Photonics Rev.* **2011**, *5*, 102−113.

(42) Liebel, M.; Schnedermann, C.; Bassolino, G.; Taylor, G.; Watts, A.; Kukura, P. Direct observation of the coherent nuclear response after the absorption of a photon. *Phys. Rev. Lett.* **2014**, *112*, 238301.

(43) Schnedermann, C.; Liebel, M.; Kukura, P. Mode-specificity of vibrationally coherent internal conversion in rhodopsin during the primary visual event. *J. Am. Chem. Soc.* **2015**, *137*, 2886−2891.

(44) Kobayashi, Y.; Chang, K. F.; Zeng, T.; Neumark, D. M.; Leone, S. R. Direct mapping of curve-crossing dynamics in IBr by attosecond transient absorption spectroscopy. *Science* **2019**, *365*, 79−83.

(45) Chang, K. F.; Wang, H.; Poullain, S. M.; Prendergast, D.; Neumark, D. M.; Leone, S. R. Mapping wave packet bifurcation at a conical intersection in CH3I by attosecond XUV transient absorption spectroscopy. *J. Phys. Chem. A* **2021**, *154*, 234301.

(46) Hua, W.; Oesterling, S.; Biggs, J. D.; Zhang, Y.; Ando, H.; de Vivie-Riedle, R.; Fingerhut, B. P.; Mukamel, S. Monitoring conical intersections in the ring opening of furan by attosecond stimulated X-ray Raman spectroscopy. *Struct. Dyn.* **2016**, *3*, 023601.

(47) Jadoun, D.; Kowalewski, M. Time-Resolved Photoelectron Spectroscopy of Conical Intersections with Attosecond Pulse Trains. *J. Phys. Chem. Lett.* **2021**, *12*, 8103−8108.

(48) Bækhøj, J. E.; Lévêque, C.; Madsen, L. B. Signatures of a conical intersection in attosecond transient absorption spectroscopy. *Phys. Rev. Lett.* **2018**, *121*, 023203.

(49) Timmers, H.; Zhu, X.; Li, Z.; Kobayashi, Y.; Sabbar, M.; Hollstein, M.; Reduzzi, M.; Martínez, T. J.; Neumark, D. M.; Leone, S. R. Disentangling conical intersection and coherent molecular dynamics in methyl bromide with attosecond transient absorption spectroscopy. *Nat. Commun.* **2019**, *10*, 3133.

(50) Meyer, H.-D.; Gatti, F.; Worth, G. A. *Multidimensional quantum dynamics: MCTDH theory and applications*; John Wiley & Sons, 2009.

(51) Meyer, H.-D.; Manthe, U.; Cederbaum, L. S. The multi-configurational time-dependent Hartree approach. *Chem. Phys. Lett.* **1990**, *165*, 73−78.

(52) Worth, G. A.; Meyer, H.-D.; Köppel, H.; Cederbaum, L.; Burghardt, I. Using the MCTDH wavepacket propagation method to describe multimode non-adiabatic dynamics. *Int. Rev. Phys. Chem.* **2008**, *27*, 569−606.

(53) Kirrander, A.; Vacher, M. Ehrenfest Methods for Electron and Nuclear Dynamics. *Quantum Chemistry and Dynamics of Excited States: Methods and Applications*; Wiley, 2020, pp 469−497.

(54) Crespo-Otero, R.; Barbatti, M. Recent advances and perspectives on nonadiabatic mixed quantum−classical dynamics. *Chem. Rev.* **2018**, *118*, 7026−7068.

(55) Li, X.; Tully, J. C.; Schlegel, H. B.; Frisch, M. J. Ab initio Ehrenfest dynamics. *J. Phys. Chem. A* **2005**, *123*, 084106.

(56) Tully, J. C. Molecular dynamics with electronic transitions. *J. Phys. Chem.* **1990**, *93*, 1061−1071.

(57) Granucci, G.; Persico, M. Critical appraisal of the fewest switches algorithm for surface hopping. *J. Phys. Chem. A* **2007**, *126*, 134114.

(58) Schmidt, J.; Parandekar, P. V.; Tully, J. C. Mixed quantum-classical equilibrium: Surface hopping. *J. Phys. Chem. A* **2008**, *129*, 044104.

(59) Preston, R. K.; Tully, J. C. Effects of surface crossing in chemical reactions: the H3+ system. *J. Phys. Chem.* **1971**, *54*, 4297−4304.

(60) Tully, J. C.; Preston, R. K. Trajectory surface hopping approach to nonadiabatic molecular collisions: the reaction of H+ with D2. *J. Phys. Chem.* **1971**, *55*, 562−572.

(61) Donati, G.; Lingerfelt, D. B.; Petrone, A.; Rega, N.; Li, X. Watching" Polaron Pair Formation from First-Principles Electron−Nuclear Dynamics. *J. Phys. Chem. A* **2016**, *120*, 7255−7261.

(62) Toldo, J. M.; do Casal, M. T.; Barbatti, M. Mechanistic Aspects of the Photophysics of UVA Filters Based on Meldrum Derivatives. *J. Phys. Chem. A* **2021**, *125*, 5499−5508.

(63) Goings, J. J.; Lingerfelt, D. B.; Li, X. Can quantized vibrational effects be obtained from Ehrenfest mixed quantum-classical dynamics? *J. Phys. Chem. Lett.* **2016**, *7*, 5193−5197.

(64) Lingerfelt, D. B.; Williams-Young, D. B.; Petrone, A.; Li, X. Direct ab initio (meta-) surface-hopping dynamics. *J. Chem. Theory Comput.* **2016**, *12*, 935−945.

(65) Petrone, A.; Donati, G.; Caruso, P.; Rega, N. Understanding THz and IR Signals Beneath Time-Resolved Fluorescence from Excited-State Ab Initio Dynamics. *J. Am. Chem. Soc.* **2014**, *136*, 14866−14874.

(66) Donati, G.; Petrone, A.; Caruso, P.; Rega, N. The Mechanism of a Green Fluorescent Protein Proton Shuttle Unveiled in the Time-Resolved Frequency Domain by Excited State Ab Initio Dynamics. *Chem. Sci.* **2018**, *9*, 1126−1135.

(67) Chiariello, M. G.; Raucci, U.; Coppola, F.; Rega, N. Unveiling Anharmonic Coupling by Means of Excited State Ab-Initio Dynamics: Application to Diarylethene Photoreactivity. *Phys. Chem. Chem. Phys.* **2019**, *21*, 3606−3614.

(68) Chiariello, M. G.; Rega, N. Exploring Nuclear Photorelaxation of Pyranine in Aqueous Solution: an Integrated Ab-Initio Molecular Dynamics and Time Resolved Vibrational Analysis Approach. *J. Phys. Chem. A* **2018**, *122*, 2884−2893.

(69) Coppola, F.; Cimino, P.; Raucci, U.; Chiariello, M. G.; Petrone, A.; Rega, N. Exploring the Franck−Condon region of a photoexcited charge transfer complex in solution to interpret femtosecond stimulated Raman spectroscopy: excited state electronic structure methods to unveil non-radiative pathways. *Chem. Sci.* **2021**, *12*, 8058−8072.

(70) Coppola, F.; Cimino, P.; Perrella, F.; Crisci, L.; Petrone, A.; Rega, N. Electronic and Vibrational Manifold of Tetracyanoethylene−Chloronaphthalene Charge Transfer Complex in Solution: Insights from TD-DFT and Ab Initio Molecular Dynamics. *J. Phys. Chem. A* **2022**, *126*, 7179−7192.

(71) Donati, G.; Petrone, A.; Rega, N. Multiresolution continuous wavelet transform for studying coupled solute−solvent vibrations via ab initio molecular dynamics. *Phys. Chem. Chem. Phys.* **2020**, *22*, 22645−22661.

(72) Schlegel, H. B.; Millam, J. M.; Iyengar, S. S.; Voth, G. A.; Daniels, A. D.; Scuseria, G. E.; Frisch, M. J. Ab initio molecular dynamics: propagating the density matrix with gaussian orbitals. *J. Chem. Phys.* **2001**, *114*, 9758−9763.

(73) Schlegel, H. B.; Iyengar, S. S.; Li, X.; Millam, J. M.; Voth, G. A.; Scuseria, G. E.; Frisch, M. J. Ab initio molecular dynamics: propagating the density matrix with gaussian orbitals. III. Comparison with Born−Oppenheimer dynamics. *J. Phys. Chem. A* **2002**, *117*, 8694−8704.

(74) Iyengar, S. S.; Schlegel, H. B.; Voth, G. A.; Millam, J. M.; Scuseria, G. E.; Frisch, M. J. Ab initio molecular dynamics: propagating the density matrix with gaussian orbitals. IV. Formal analysis of the deviations from Born-Oppenheimer dynamics. *Isr. J. Chem.* **2002**, *42*, 191−202.

(75) Schlegel, H. B. Ab initio molecular dynamics with Born-Oppenheimer and Extended Lagrangian methods using atom centered basis functions. *Bull. Korean Chem. Soc.* **2003**, *24*, 837−842.

(76) Rega, N.; Iyengar, S. S.; Voth, G. A.; Schlegel, H. B.; Vreven, T.; Frisch, M. J. Hybrid Ab-initio/empirical molecular dynamics: combining the ONIOM scheme with the atom-centered density matrix propagation (ADMP) approach. *J. Phys. Chem. B* **2004**, *108*, 4210−4220.

(77) Millam, J. M.; Bakken, V.; Chen, W.; Hase, W. L.; Schlegel, H. B. Ab Initio Classical Trajectories on the Born−Oppenheimer Surface: Hessian-Based Integrators using Fifth-order Polynomial and Rational Function Fits. *J. Chem. Phys.* **1999**, *111*, 3800−3805.

(78) Bolton, K.; Hase, W. L.; Peslherbe, G. H. *Modern Methods for Multidimensional Dynamics Computations in Chemistry*; World Scientific, 1998; pp 143−189.

(79) Daubechies, I.; Daubechies, I. Ten Lectures on Wavelets. *Siam* **1993**, *61*, 941.

(80) Torrence, C.; Compo, G. P. A Practical Guide to Wavelet Analysis. *Bull. Am. Meteorol. Soc.* **1998**, *79*, 61−78.

(81) Chiariello, M. G.; Donati, G.; Rega, N. Time-Resolved vibrational analysis of excited state ab initio molecular dynamics to understand photorelaxation: The case of the pyranine photoacid in aqueous solution. *J. Chem. Theory Comput.* **2020**, *16*, 6007−6013.

(82) Melby, L.; Harder, R.; Hertler, W.; Mahler, W.; Benson, R.; Mochel, W. Substituted quinodimethans. II. Anion-radical derivatives and complexes of 7, 7, 8, 8-tetracyanoquinodimethan. *J. Am. Chem. Soc.* **1962**, *84*, 3374−3387.

(83) Ferraris, J.; Cowan, D.; Walatka, V. t.; Perlstein, J. Electron Transfer in a New Highly Conducting Donor-Acceptor Complex. *J. Am. Chem. Soc.* **1973**, *95*, 948−949.

(84) Cohen, M. J.; Coleman, L.; Garito, A.; Heeger, A. Electrical conductivity of tetrathiofulvalinium tetracyanoquinodimethan (TTF)-(TCNQ). *Phys. Rev. B* **1974**, *10*, 1298−1307.

(85) Saito, G.; Murata, T. Mixed Valency in Organic Charge Transfer Complexes. *Philos. Trans. R. Soc., A* **2008**, *366*, 139−150.

(86) Torrance, J. B. The difference between metallic and insulating salts of tetracyanoquinodimethone (TCNQ): how to design an organic metal. *Acc. Chem. Res.* **1979**, *12*, 79−86.

(87) Tseng, T.-C.; Urban, C.; Wang, Y.; Otero, R.; Tait, S. L.; Alcamí, M.; Écija, D.; Trelka, M.; Gallego, J. M.; Lin, N.; et al. Charge-transfer-induced structural rearrangements at both sides of organic/metal interfaces. *Nat. Chem.* **2010**, *2*, 374−379.

(88) Kaplunov, M. G.; Panova, T. P.; Yagubskii, E. B.; Borod'ko, Y. G. The vibrational spectra of tetracyanoquinodimethane and its complexes. *J. Struct. Chem.* **1972**, *13*, 411−417.

(89) Tamaya, H.; Torii, Y.; Ishikawa, T.; Nakano, H.; Iimori, T. Photophysics and Inverted Solvatochromism of 7,7,8,8-Tetracyano-quinodimethane (TCNQ). *ChemPhysChem* **2019**, *20*, 2531−2538.

(90) Otero, R.; Miranda, R.; Gallego, J. M. A Comparative Computational Study of the Adsorption of TCNQ and F4-TCNQ on the Coinage Metal Surfaces. *ACS Omega* **2019**, *4*, 16906−16915.

(91) Hoffman, D. P.; Ellis, S. R.; Mathies, R. A. Characterization of a Conical Intersection in a Charge-Transfer Dimer with Two-Dimensional Time-Resolved Stimulated Raman Spectroscopy. *J. Phys. Chem. A* **2014**, *118*, 4955−4965.

(92) Berera, R.; van Grondelle, R.; Kennis, J. T. Ultrafast Transient Absorption Spectroscopy: Principles and Application to Photo-synthetic Systems. *Photosynth. Res.* **2009**, *101*, 105−118.

(93) Petrone, A.; Perrella, F.; Coppola, F.; Crisci, L.; Donati, G.; Cimino, P.; Rega, N. Ultrafast photo-induced processes in complex environments: The role of accuracy in excited-state energy potentials and initial conditions. *Chem. Phys. Rev.* **2022**, *3*, 021307.

(94) Gaigeot, M.-P.; Martinez, M.; Vuilleumier, R. Infrared spectroscopy in the gas and liquid phase from first principle molecular dynamics simulations: application to small peptides. *Mol. Phys.* **2007**, *105*, 2857−2878.

(95) Gaigeot, M. P.; Vuilleumier, R.; Sprik, M.; Borgis, D. Infrared spectroscopy of N-MethylAcetamide revisited by ab initio molecular dynamics simulations. *J. Chem. Theory Comput.* **2005**, *1*, 772−789.

(96) Buchner, M.; Ladanyi, B. M.; Stratt, R. M. The short-time dynamics of molecular liquids. Instantaneous-normal-mode theory. *J. Chem. Phys.* **1992**, *97*, 8522−8535.

(97) Cho, M.; Fleming, G. R.; Saito, S.; Ohmine, I.; Stratt, R. M. Instantaneous normal mode analysis of liquid water. *J. Chem. Phys.* **1994**, *100*, 6672−6683.

(98) Goodyear, G.; Stratt, R. M. The short-time intramolecular dynamics of solutes in liquids. I. An instantaneous-normal-mode theory for friction. *J. Chem. Phys.* **1996**, *105*, 10050−10071.

(99) Stratt, R. M. The instantaneous normal modes of liquids. *Acc. Chem. Res.* **1995**, *28*, 201−207.

(100) Rega, N. Vibrational Analysis beyond the Harmonic Regime from Ab-Initio Molecular Dynamics. *Theor. Chem. Acc.* **2006**, *116*, 347−354.

(101) Strachan, A. Normal modes and frequencies from covariances in molecular dynamics or Monte Carlo simulations. *J. Chem. Phys.* **2004**, *120*, 1−4.

(102) Schmitz, M.; Tavan, P. Vibrational spectra from atomic fluctuations in dynamics simulations. I. Theory, limitations, and a sample application. *J. Chem. Phys.* **2004**, *121*, 12233−12246.

(103) Schmitz, M.; Tavan, P. Vibrational spectra from atomic fluctuations in dynamics simulations. II. Solvent-induced frequency fluctuations at femtosecond time resolution. *J. Chem. Phys.* **2004**, *121*, 12247−12258.

(104) Martinez, M.; Gaigeot, M.-P.; Borgis, D.; Vuilleumier, R. Extracting effective normal modes from equilibrium dynamics at finite temperature. *J. Chem. Phys.* **2006**, *125*, 144106.

(105) Thomas, M.; Brehm, M.; Fligg, R.; Vöhringer, P.; Kirchner, B. Computing vibrational spectra from ab initio molecular dynamics. *Phys. Chem. Chem. Phys.* **2013**, *15*, 6608−6622.

(106) Heidari, Z.; Roe, D. R.; Galindo-Murillo, R.; Ghasemi, J. B.; Cheatham, T. E. Using wavelet analysis to assist in identification of significant events in molecular dynamics simulations. *J. Chem. Inf. Model.* **2016**, *56*, 1282−1291.

(107) Pagliai, M.; Muniz-Miranda, F.; Cardini, G.; Righini, R.; Schettino, V. Hydrogen bond dynamics of methyl acetate in methanol. *J. Phys. Chem. Lett.* **2010**, *1*, 2951−2955.

(108) Otsuka, T.; Nakai, H. Wavelet transform analysis of ab initio molecular dynamics simulation: Application to core-excitation dynamics of BF3. *J. Comput. Chem.* **2007**, *28*, 1137−1144.

(109) Rahaman, A.; Wheeler, R. A. Wavelet transforms for determining time-dependent vibrational frequencies. *J. Chem. Theory Comput.* **2005**, *1*, 769−771.

(110) Mallat, S. *A Wavelet Tour of Signal Processing*; Elsevier, 1999.

(111) Becke, A. D. Density-Functional Thermochemistry. III. The Role of Exact Exchange. *J. Chem. Phys.* **1993**, *98*, 5648−5652.

(112) Lee, C.; Yang, W.; Parr, R. G. Development of the Colle-Salvetti Correlation-Energy Formula into a Functional of the Electron Density. *Phys. Rev. B* **1988**, *37*, 785−789.

(113) Miehlich, B.; Savin, A.; Stoll, H.; Preuss, H. Results Obtained with the Correlation Energy Density Functionals of Becke and Lee, Yang and Parr. *Chem. Phys. Lett.* **1989**, *157*, 200−206.

(114) Yanai, T.; Tew, D. P.; Handy, N. C. A New Hybrid Exchange−Correlation Functional Using the Coulomb-Attenuating Method (CAM-B3LYP). *Chem. Phys. Lett.* **2004**, *393*, 51−57.

(115) Kobayashi, R.; Amos, R. D. The Application of CAM-B3LYP to the Charge-Transfer Band Problem of the Zincbacteriochlorin−bacteriochlorin Complex. *Chem. Phys. Lett.* **2006**, *420*, 106−109.

(116) Cai, Z.-L.; Crossley, M. J.; Reimers, J. R.; Kobayashi, R.; Amos, R. D. Density Functional Theory for Charge Transfer: the Nature of the N-bands of Porphyrins and Chlorophylls Revealed Through CAM-B3LYP, CASPT2, and SAC-CI Calculations. *J. Phys. Chem. B* **2006**, *110*, 15624−15632.

(117) Rostov, I. V.; Amos, R. D.; Kobayashi, R.; Scalmani, G.; Frisch, M. J. Studies of the ground and excited-state surfaces of the retinal chromophore using CAM-B3LYP. *J. Phys. Chem. B* **2010**, *114*, 5547−5555.

(118) Li, R.; Zheng, J.; Truhlar, D. G. Density Functional Approximations for Charge Transfer Excitations with Intermediate Spatial Overlap. *Phys. Chem. Chem. Phys.* **2010**, *12*, 12697−12701.

(119) Petersilka, M.; Gossmann, U.; Gross, E. Excitation Energies from Time-Dependent Density-Functional Theory. *Phys. Rev. Lett.* **1996**, *76*, 1212−1215.

(120) Champagne, B.; Perpète, E. A.; van Gisbergen, S. J.; Baerends, E.-J.; Snijders, J. G.; Soubra-Ghaoui, C.; Robins, K. A.; Kirtman, B.

Assessment of Conventional Density Functional Schemes for Computing the Polarizabilities and Hyperpolarizabilities of Conjugated Oligomers: an Ab Initio Investigation of Polyacetylene Chains. *J. Chem. Phys.* **1998**, *109*, 10489−10498.

(121) Dreuw, A.; Head-Gordon, M. Failure of Time-Dependent Density Functional Theory for Long-Range Charge-Transfer Excited States: the Zincbacteriochlorin-Bacteriochlorin and Bacteriochlorophyll-Spheroidene Complexes. *J. Am. Chem. Soc.* **2004**, *126*, 4007−4016.

(122) Magyar, R.; Tretiak, S. Dependence of Spurious Charge-Transfer Excited States on Orbital Exchange in TDDFT: Large Molecules and Clusters. *J. Chem. Theory Comput.* **2007**, *3*, 976−987.

(123) Peach, M. J.; Benfield, P.; Helgaker, T.; Tozer, D. J. Excitation Energies in Density Functional Theory: an Evaluation and a Diagnostic Test. *J. Chem. Phys.* **2008**, *128*, 044118.

(124) Dwyer, A. D.; Tozer, D. J. Effect of Chemical Change on TDDFT Accuracy: Orbital Overlap Perspective of the Hydrogenation of Retinal. *Phys. Chem. Chem. Phys.* **2010**, *12*, 2816−2818.

(125) Iikura, H.; Tsuneda, T.; Yanai, T.; Hirao, K. A Long-Range Correction Scheme for Generalized-Gradient-Approximation Exchange Functionals. *J. Chem. Phys.* **2001**, *115*, 3540−3544.

(126) Stein, T.; Kronik, L.; Baer, R. Prediction of Charge-transfer Excitations in Coumarin-Based Dyes Using a Range-Separated Functional Tuned from First Principles. *J. Chem. Phys.* **2009**, *131*, 244119.

(127) Wong, B. M.; Piacenza, M.; Sala, F. D. Absorption and Fluorescence Properties of Oligothiophene Biomarkers from Long-Range-Corrected Time-Dependent Density Functional Theory. *Phys. Chem. Chem. Phys.* **2009**, *11*, 4498−4508.

(128) Mardirossian, N.; Parkhill, J. A.; Head-Gordon, M. Benchmark results for empirical post-GGA functionals: Difficult exchange problems and independent tests. *Phys. Chem. Chem. Phys.* **2011**, *13*, 19325−19337.

(129) Laurent, A. D.; Jacquemin, D. TD-DFT Benchmarks: a Review. *Int. J. Quantum Chem.* **2013**, *113*, 2019−2039.

(130) Derian, R.; Tokar, K.; Somogyi, B.; Gali, A.; Stich, I. Optical gaps in pristine and heavily doped silicon nanocrystals: DFT versus quantum Monte Carlo benchmarks. *J. Chem. Theory Comput.* **2017**, *13*, 6061−6067.

(131) Petrone, A.; Beck, R. A.; Kasper, J. M.; Li, X.; Huang, Y.; Crane, M.; Pauzauskie, P. Electronic structures and spectroscopic signatures of silicon-vacancy containing nanodiamonds. *Phys. Rev. B* **2018**, *98*, 205405.

(132) Perdew, J. P.; Ernzerhof, M.; Burke, K. Rationale for Mixing Exact Exchange with Density Functional Approximations. *J. Chem. Phys.* **1996**, *105*, 9982−9985.

(133) Adamo, C.; Barone, V. Toward Reliable Density Functional Methods without Adjustable Parameters: the PBE0Model. *J. Chem. Phys.* **1999**, *110*, 6158−6170.

(134) Grimme, S.; Ehrlich, S.; Goerigk, L. Effect of the Damping Function in Dispersion Corrected Density Functional Theory. *J. Comput. Chem.* **2011**, *32*, 1456−1465.

(135) Grimme, S. Density Functional Theory with London Dispersion Corrections. *Wiley Interdiscip. Rev.: Comput. Mol. Sci.* **2011**, *1*, 211−228.

(136) Grimme, S.; Antony, J.; Ehrlich, S.; Krieg, H. A Consistent and Accurate Ab Initio Parametrization of Density Functional Dispersion Correction (DFT-D) for the 94 Elements H-Pu. *J. Chem. Phys.* **2010**, *132*, 154104.

(137) Ehrlich, S.; Moellmann, J.; Grimme, S. Dispersion-corrected density functional theory for aromatic interactions in complex systems. *Acc. Chem. Res.* **2013**, *46*, 916−926.

(138) Risthaus, T.; Grimme, S. Benchmarking of London Dispersion-Accounting Density Functional Theory Methods on Very Large Molecular Complexes. *J. Chem. Theory Comput.* **2013**, *9*, 1580−1591.

(139) Grimme, S. Do Special Noncovalent π−π Stacking Interactions Really Exist? *Angew. Chem., Int. Ed.* **2008**, *47*, 3430−3434.

(140) Frisch, M. J.; Trucks, G. W.; Schlegel, H. B.; Scuseria, G. E.; Robb, M. A.; Cheeseman, J. R.; Scalmani, G.; Barone, V.; Petersson, G. A.; Nakatsuji, H.; Li, X.; Caricato, M.; Marenich, A. V.; Bloino, J.; Janesko, B. G.; Gomperts, R.; Mennucci, B.; Hratchian, H. P.; Ortiz, J. V.; Izmaylov, A. F.; Sonnenberg, J. L.; Williams-Young, D.; Ding, F.; Lipparini, F.; Egidi, F.; Goings, J.; Peng, B.; Petrone, A.; Henderson, T.; Ranasinghe, D.; Zakrzewski, V. G.; Gao, J.; Rega, N.; Zheng, G.; Liang, W.; Hada, M.; Ehara, M.; Toyota, K.; Fukuda, R.; Hasegawa, J.; Ishida, M.; Nakajima, T.; Honda, Y.; Kitao, O.; Nakai, H.; Vreven, T.; Throssell, K.; Montgomery, J. A., Jr; Peralta, J. E.; Ogliaro, F.; Bearpark, M. J.; Heyd, J. J.; Brothers, E. N.; Kudin, K. N.; Staroverov, V. N.; Keith, T. A.; Kobayashi, R.; Normand, J.; Raghavachari, K.; Rendell, A. P.; Burant, J. C.; Iyengar, S. S.; Tomasi, J.; Cossi, M.; Millam, J. M.; Klene, M.; Adamo, C.; Cammi, R.; Ochterski, J. W.; Martin, R. L.; Morokuma, K.; Farkas, O.; Foresman, J. B.; Fox, D. J. *Gaussian16*, Revision A.06.; Gaussian Inc: Wallingford CT, 2016.